

**Supplementary Information for:**  
**Automated high-throughput Wannierisation**

Valerio Vitale,<sup>1,2,\*</sup> Giovanni Pizzi,<sup>3</sup> Antimo Marrazzo,<sup>3</sup>  
Jonathan R. Yates,<sup>4</sup> Nicola Marzari,<sup>3</sup> and Arash A. Mostofi<sup>2</sup>

<sup>1</sup>*Cavendish Laboratory, Department of Physics,  
University of Cambridge, 19 JJ Thomson Avenue Cambridge UK*

<sup>2</sup>*Departments of Materials and Physics,  
and the Thomas Young Centre for Theory and Simulation of Materials,  
Imperial College London, London SW7 2AZ, UK*

<sup>3</sup>*Theory and Simulation of Materials (THEOS) and National Centre for  
Computational Design and Discovery of Novel Materials (MARVEL),  
École Polytechnique Fédérale de Lausanne, Lausanne, Switzerland*

<sup>4</sup>*Department of Materials, University of Oxford, Parks Road, Oxford OX1 3PH, UK*

(Dated: February 28, 2020)

# Supplementary Methods

## SCDM implementation in Quantum ESPRESSO

To implement the SCDM method one needs the wavefunctions from the *ab initio* code represented on a real space grid, see Eq. (14) in the main text. Since these are not directly accessible to WANNIER90, we decided to implement the method in one of the open-source DFT-to-WANNIER90 interface packages available. In particular, we have chosen the PW2WANNIER90 FORTRAN code, distributed with the open-source QUANTUM ESPRESSO suite.<sup>1</sup> Our SCDM implementation is available since the v6.3 release of QUANTUM ESPRESSO. It includes the extension of the method to  $k$ -points and to entangled bands, and it is parallelised using the Message Passing Interface (MPI).

To compute the  $A_{mn}^{(\mathbf{k})}$  projection matrices using SCDM, the `auto_projections` keyword must be set to `.true.` in the WANNIER90 input file. In addition, the following keywords should be defined in the PW2WANNIER90 input file: `scdm_proj`, `scdm_entanglement`, `scdm_mu` and `scdm_sigma`. In particular, `scdm_proj` is a boolean flag to enable the SCDM method. `scdm_entanglement` is a string defining the functional form of the  $f(\varepsilon)$  function in Eq. (15) in the main text. In the cases described in this paper, the value is either `isolated` (isolated bands) or `erfc` (entangled bands with the  $f(\varepsilon)$  of Eq. (16) in the main text). An additional choice we implemented is `gaussian`, see Ref. [2] for its functional form. Finally, `scdm_mu` and `scdm_sigma` (not needed if `scdm_entanglement` is `isolated`) define, respectively, the values of  $\mu$  and  $\sigma$  (in eV) in Eq. (16) in the main text.

In PW2WANNIER90, the QRCP factorisation of the  $\Psi_{\mathbf{k}=\Gamma}^\dagger$  matrix is obtained through the LAPACK routine ZGEP3. Presently the factorisation is performed on a single MPI process (since ZGEP3 is not available in the parallel ScaLAPACK routines) and the resulting permutation matrix  $\Pi$  is broadcast to all processes. After the computation of the non-orthogonal SCDM functions, a Löwdin orthogonalisation is performed. This step is not needed when providing the  $A_{mn}^{(\mathbf{k})}$  matrices to WANNIER90, since the same orthogonalisation is performed by the code before the start of the minimisation. However, having the orthogonalisation step also in the PW2WANNIER90 interface allows users to directly employ the SCDM functions without further processing, if needed.

As a final note, we emphasise that when ultrasoft pseudopotentials are employed, the  $\psi_{n\mathbf{k}}(\mathbf{r})$  wavefunctions satisfy a generalised orthogonality condition with a non-trivial metric  $\hat{S}$  being a function of the core augmentation charges.<sup>3</sup> In this case the  $u_{n\mathbf{k}}$  stored by QUANTUM ESPRESSO are not orthonormal, resulting in  $\Psi$  being non unitary. However, in practice this usually has only

a marginal effect on the results. Indeed, as we have shown, the algorithm manages to find good Wannier functions also when employing ultrasoft pseudopotentials and therefore no adaptation has been applied for the ultrasoft case.

### Properties of the QRCP factorisation

We recall in this section the properties of the  $Q$ ,  $R$ , and  $\Pi$  matrices obtained from a QRCP decomposition, in the general case where the matrix to decompose is rectangular. For definiteness, we consider the decomposition of a rectangular  $\Psi^\dagger$  matrix of shape  $J \times n_G$ .

The QRCP decomposition can be written as:

$$\Psi^\dagger \Pi = QR \tag{S1}$$

where the matrices have the following properties:

1.  $Q$  is a  $J \times J$  unitary matrix, i.e., it has orthonormal columns:  $Q^\dagger Q = \mathbf{1}_J$ ;
2.  $\Pi$  is a  $n_G \times n_G$  permutation matrix (permuting the columns of  $\Psi^\dagger$ );
3.  $R$  is an upper-triangular rectangular matrix of shape  $J \times n_G$ , with diagonal elements sorted with decreasing absolute value:  $|R_{11}| \geq |R_{22}| \geq \dots \geq |R_{JJ}|$  (this order is ensured thanks to the action of the  $\Pi$  matrix).

### QRCP column selection of $P$ from the column selection of $\Psi^\dagger$

We consider a  $n_G \times n_G$  matrix  $P$  that can be written in the following form  $P = \Psi \Psi^\dagger$ , with  $\Psi$  being a  $n_G \times J$  matrix ( $J < n_G$ ) with orthonormal columns, i.e.  $\Psi^\dagger \Psi = \mathbf{1}_J$ . We want to show that if we consider the following QRCP decomposition for  $\Psi^\dagger$ :

$$\Psi^\dagger \Pi = QR, \tag{S2}$$

then we can construct a QRCP decomposition for  $P$  having the same permutation matrix  $\Pi$ :

$$P \Pi = Q' R'. \tag{S3}$$

Let us start by multiplying Eq. (S2) on the left by  $\Psi$ :

$$P \Pi \equiv \Psi \Psi^\dagger \Pi = (\Psi Q) R \equiv Q' R, \tag{S4}$$

where we have defined  $Q' \equiv \Psi Q$ .

Let us first verify that  $Q'$  has orthonormal columns:

$$(Q')^\dagger Q' = (Q^\dagger \Psi^\dagger)(\Psi Q) = Q^\dagger Q = \mathbf{1}_J, \quad (\text{S5})$$

where we have used the orthonormality of the columns of  $\Psi$  (by hypothesis) and of  $Q$  (since it is the output of a QRCP algorithm, see point 1 in ).

Let us now define the following  $n_G \times n_G$  matrices:

$$Q'' \equiv \left( Q' \mid \tilde{Q} \right), \quad R'' \equiv \begin{pmatrix} R \\ \mathbf{0}_{(n_G-J) \times n_G} \end{pmatrix}, \quad (\text{S6})$$

where  $\left( A \mid B \right)$  means horizontal concatenation of matrix  $A$  with matrix  $B$ , where  $A$  and  $B$  must have the same number of rows, and  $\begin{pmatrix} A \\ B \end{pmatrix}$  means vertical concatenation ( $A$  and  $B$  must have same number of columns). the additional columns  $\tilde{Q}$  of  $Q''$  are chosen to complete the columns of  $Q'$  to an orthonormal basis of  $\mathbb{R}^{n_G}$  (always possible) and  $R''$  extends  $R$  with  $(n_G - J)$  additional rows of zeros.

We want now to prove that  $P\Pi = Q''R''$  is a QRCP decomposition of  $P$ . Indeed, by multiplying by blocks the two matrices  $Q''$  and  $R''$ , we get  $Q''R'' = Q'R + \tilde{Q}\mathbf{0} = Q'R = P\Pi$  by virtue of Eq. (S4). Moreover,  $Q''$  is a unitary matrix by construction, and  $R''$  is clearly an upper-triangular matrix since  $R$  is according to point 3 of , and the diagonal elements are still sorted in decreasing magnitude order since the additional elements are all zero. Therefore, we have shown that the same permutation matrix  $\Pi$  obtained by applying the QRCP to  $\Psi^\dagger$  is a valid QRCP permutation matrix also for  $P$ .

A different, equivalent approach to show the same result is to observe that the (complex) scalar product  $\mathbf{v}_1 \cdot \mathbf{v}_2 \equiv (\mathbf{v}_1^*)^T \mathbf{v}_2$  between columns of  $P$  is the same as the scalar product of the columns of  $\Psi^\dagger$ . Indeed, we first note that, as it can be easily proven from its explicit expression Eq. (12) in the main text,  $P$  is a projector and it holds that  $P^2 = P$  and  $P^\dagger = P$ . Therefore, we have  $P^\dagger P = P$ . But the elements of  $P^\dagger P$  are nothing else than the scalar products of the columns of  $P$ , and therefore  $P_{ij} = \mathbf{p}_i \cdot \mathbf{p}_j$ , with  $\mathbf{p}_i$  indicating the  $i$ -th column of  $P$ . At the same time, from the definition of  $P = \Psi\Psi^\dagger = (\Psi^\dagger)^\dagger \Psi^\dagger$  we immediately notice that the elements of  $P$  are also the scalar products of the columns of  $\Psi^\dagger$ , i.e. the complex conjugate  $\psi_i^*$  of the wavefunctions of the system, proving our statement that

$$P_{ij} = \mathbf{p}_i \cdot \mathbf{p}_j = (\langle \psi_i | \psi_j \rangle)^*. \quad (\text{S7})$$

## Geometrical interpretation of the column selection in the QRCP algorithm

QRCP is a greedy algorithm, where the  $\Pi$  matrix is constructed by picking the columns one by one to obtain the condition  $|R_{11}| \geq |R_{22}| \geq \dots \geq |R_{JJ}|$ . In the case of the QRCP decomposition of a  $P$  matrix, the first column to be picked  $(\mathbf{p}_1)_i \equiv (P\Pi)_{i1}$  is chosen as the one with largest norm. This can be easily proven by noting that

$$(P\Pi)_{i1} = (QR)_{i1} = Q_{i1}R_{11},$$

because of the triangular form of  $R$ . Moreover, since the columns of  $Q$  have unit norm, then  $\|\mathbf{p}_1\| = |R_{11}|$  by construction (see point 3 of ) is the largest possible.

More generally, the  $j$ -th column  $\mathbf{p}_j$  is chosen to maximise the norm of the component  $\mathbf{p}_j^\perp$  orthogonal to the subspace  $\mathcal{S}_{j-1}$  spanned by the previous  $(j-1)$  columns. To prove this, let us first write  $\mathbf{p}_j = \mathbf{p}_j^\parallel + \mathbf{p}_j^\perp$ , where  $\mathbf{p}_j^\parallel$  is the projection of  $\mathbf{p}_j$  within  $\mathcal{S}_{j-1}$ . We first note (again due to the triangular form of  $R$ ) that in general the first  $j$  columns of  $Q$  also span the space  $\mathcal{S}_j$  and, moreover, they are a orthonormal basis set for  $\mathcal{S}_j$  since the  $Q$  columns are orthonormal. Furthermore  $\mathbf{p}_j$  is, by definition, in the  $\mathcal{S}_j$  subspace. Therefore, we can write the  $j$ -th column in this basis set of  $\mathcal{S}_j$  as

$$(\mathbf{p}_j)_i = (P\Pi)_{ij} = (QR)_{ij} = \sum_{m=1}^j Q_{im}R_{mj},$$

and, thanks to the orthonormality of the  $\{\mathbf{q}_m\}$  basis ( $\mathbf{q}_i$  being the  $i$ -th column of  $Q$ ), we have

$$\left(\mathbf{p}_j^\parallel\right)_i = \sum_{m=1}^{j-1} Q_{im}R_{mj}, \quad \left(\mathbf{p}_j^\perp\right)_i = Q_{ij}R_{jj},$$

or equivalently in vector form  $\mathbf{p}_j^\perp = \mathbf{q}_j R_{jj}$ .

Therefore, the norm of this orthogonal component is simply  $\|\mathbf{p}_j^\perp\| = |R_{jj}|$  that, again, is chosen by the algorithm to have maximal value (in order to have decreasing diagonal elements of  $R$ ), therefore proving our intuitive explanation of the QRCP column selection.

To give a more physical interpretation of the column selection in terms of the charge density or wavefunctions, we observe that from Eq. (S7) we know that the square modulus of the  $i$ -th column of  $P$  is  $\|\mathbf{p}_i\|^2 = P_{ii}$ , and the diagonal element of  $P$  is simply  $\rho(\mathbf{r}_i)$ , i.e. the charge density at the discretised grid point  $\mathbf{r}_i$ . Therefore, the algorithm will choose the first column  $\mathbf{p}_{\Pi(1)}$  as the one corresponding to the point in space  $\mathbf{r}_i$  with maximal charge density (i.e., the projection of a delta-like function centred on  $\mathbf{r}_i$ ).

The second (and following) columns, that are projections of delta-like functions on other grid points, will then be chosen (as discussed before) so as to maximise the orthogonality of this projection with respect to the subspace defined by all previous ones. For instance, for the second vector  $\mathbf{p}_{\Pi(2)}$ , the norm of its orthogonal component to  $\mathbf{p}_{\Pi(1)}$  can be shown to be

$$\begin{aligned} \|\mathbf{p}_{\Pi(2)}^\perp\|^2 &= \|\mathbf{p}_{\Pi(2)}\|^2 - \frac{|\mathbf{p}_{\Pi(1)} \cdot \mathbf{p}_{\Pi(2)}|^2}{\|\mathbf{p}_{\Pi(1)}\|^2} = \\ &= \rho(\mathbf{r}_{\Pi(2)}) - \frac{|P_{\Pi(1)\Pi(2)}|^2}{\rho(\mathbf{r}_{\Pi(1)})}, \end{aligned} \quad (\text{S8})$$

and therefore choosing  $\Pi(2)$  to maximise it (at fixed chosen  $\Pi(1)$ ) is equivalent to maximising

$$\rho(\mathbf{r}_{\Pi(2)}) - \frac{|P_{\Pi(1)\Pi(2)}|^2}{\rho(\mathbf{r}_{\Pi(1)})}. \quad (\text{S9})$$

### Equivalence of the SCDM method with the Cholesky orbitals

We want to show here that the algorithm to obtain the Cholesky orbitals of Aquilante *et al.*<sup>4</sup> provides the same selection of columns as the QRCP prescribed by the SCDM method.

As also explained in Ref. [5], the following algorithm can be employed in order to obtain the  $k$ -th selected column  $\Pi(k)$ :

1. Define an initial matrix  $P^{(0)} = P$  being the density matrix of the system.
2. At every step  $k \geq 1$ , choose  $\Pi(k)$  as the index of the column where the matrix  $P^{(k-1)}$  has maximum diagonal element. Also, we define the  $k$ -th Cholesky vector  $\mathbf{c}_k$  as the  $\Pi(k)$ -th column of  $P^{(k-1)}$ , rescaled by the inverse square root of the corresponding diagonal element:

$$(\mathbf{c}_k)_j = \frac{1}{\sqrt{P_{\Pi(k)\Pi(k)}^{(k-1)}}} [P^{(k-1)}]_{j\Pi(k)}. \quad (\text{S10})$$

3. Define the matrix  $P^{(k)}$  for the next iteration as follows:

$$P^{(k)} = P^{(k-1)} - \mathbf{c}_k \cdot \mathbf{c}_k^\dagger \quad (\text{S11})$$

(where  $\mathbf{c}_k \cdot \mathbf{c}_k^\dagger$  indicates a matrix product).

4. Iterate the previous two points until the needed number of selected columns is obtained.

We can now show that this approach is equivalent to the selection of columns of the QRCP algorithm. In particular, in the first step, the Cholesky approach selects the column corresponding to the largest diagonal element of  $P$ , which is exactly the same choice as the QRCP algorithm, as discussed in .

At the second step ( $k = 1$ ), substituting Eq. (S10) in Eq. (S11) and using  $P^{(0)} = P$ , we have

$$\begin{aligned} P_{ij}^{(1)} &= P_{ij} - [\mathbf{c}_{\Pi(1)} \cdot \mathbf{c}_{\Pi(1)}^\dagger]_{ij} = \\ &= P_{ij} - \frac{P_{i\Pi(1)}P_{j\Pi(1)}^*}{P_{\Pi(1)\Pi(1)}} = P_{ij} - \frac{P_{i\Pi(1)}P_{j\Pi(1)}^*}{\rho(\mathbf{r}_{\Pi(1)})}. \end{aligned} \quad (\text{S12})$$

In particular, we can notice now that the diagonal elements  $P_{jj}^{(1)}$  of  $P^{(1)}$  can be written as

$$P_{jj}^{(1)} = P_{jj} - \frac{|P_{\Pi(1)j}|^2}{\rho(\mathbf{r}_{\Pi(1)})}, \quad (\text{S13})$$

(where we have used  $P^\dagger = P$ ) and therefore the choice of  $j = \Pi(2)$  based on the largest diagonal element of  $P^{(1)}$ , as prescribed by the Cholesky algorithm, is equivalent to the QRCP choice maximising Eq. (S9).

Finally, we note that the  $\Pi(1)$ -th column of  $P^{(1)}$  is composed only by zeros (and analogously for the  $\Pi(1)$ -th row since the  $P^{(i)}$  matrices are Hermitian), since

$$P_{i\Pi(1)}^{(1)} = P_{i\Pi(1)} - \frac{P_{i\Pi(1)}P_{\Pi(1)\Pi(1)}^*}{P_{\Pi(1)\Pi(1)}} = P_{i\Pi(1)} - P_{i\Pi(1)} = 0 \quad (\text{S14})$$

(where we have used the fact that the diagonal elements of  $P$  are real). This fact, in addition to providing numerical stability to the Cholesky-orbital algorithm by forcing these elements to be numerically zero, allows us to “remove” the zero row and column from  $P^{(1)}$  and repeat the reasoning by induction for all subsequent Cholesky vectors, working with smaller and smaller matrices.

Equivalently, one could understand more intuitively the result by noting that the Cholesky vectors of Eq. (S10) are normalised to 1 because of Eq. (S7). Therefore, Eq. (S11) constructs a new projection operator  $P^{(k)}$  projecting on the subspace of the span of  $P^{(k-1)}$  that is also orthogonal to  $\mathbf{c}_k$ , and then the Cholesky algorithm selects the largest vector in this subspace, that is exactly what the QRCP algorithm also does, as discussed in .

## Supplementary Note 1

In S1 we report the Wannier-interpolated valence bands and four low-lying conduction bands in silicon for three different set of initial projections (two explicit sets of projections and one using

the SCDM method).

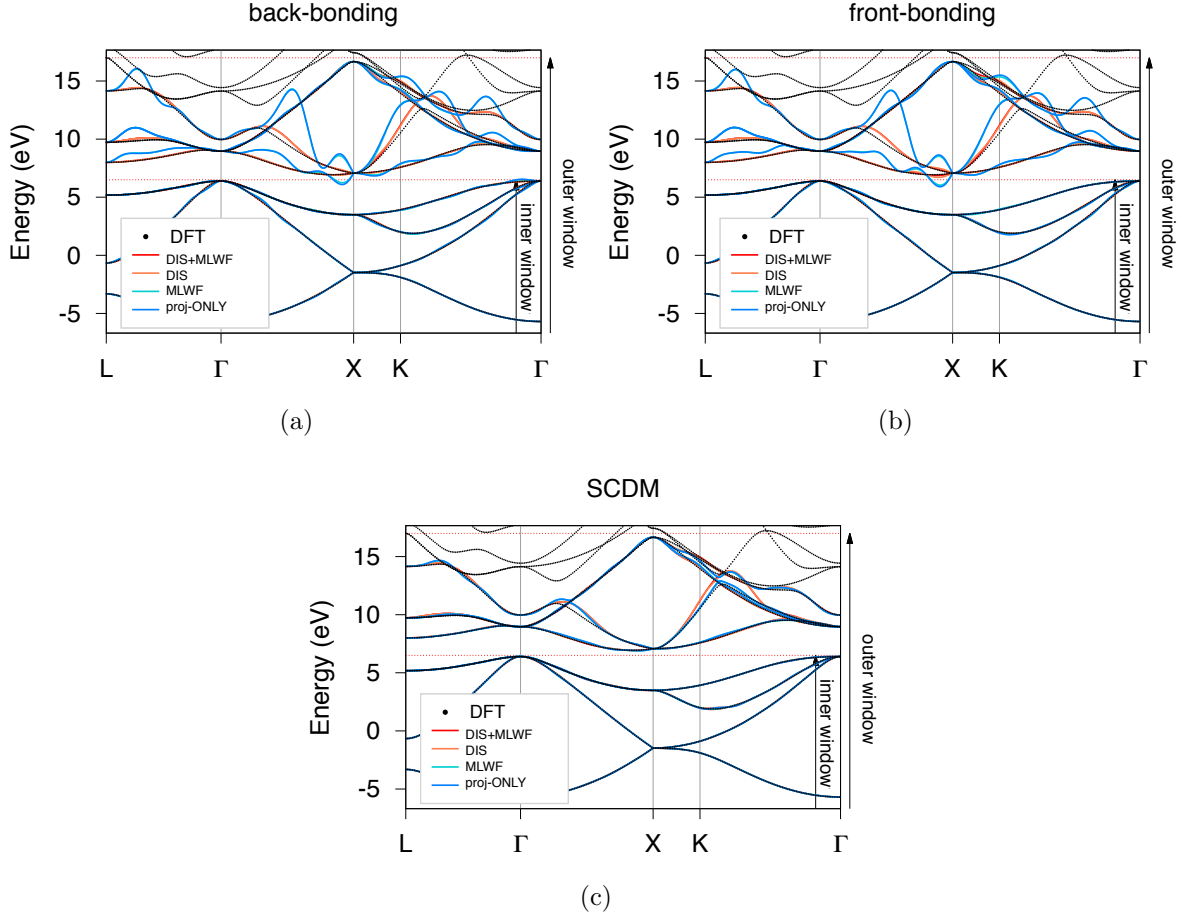


Figure S1: Wannier interpolated valence bands and four low-lying conduction bands in silicon from three different set of initial projections: a) eight  $sp^3$  in the *back-bonding* configuration; b) eight  $sp^3$  in the *front-bonding* configuration and c) from SCDM with  $\mu = 10$  eV and  $\sigma = 2$  eV. For each plot the interpolation from four minimisation schemes are shown: 1) full minimisation of  $\Omega$  (DIS+MLWF), with  $\varepsilon_{\text{outer}} = 17$  eV and  $\varepsilon_{\text{inner}} = 6.5$  eV for the disentanglement step (solid red). 2) Minimisation of  $\Omega_I$  only ”disentanglement” (DIS) with  $\varepsilon_{\text{outer}} = 17$  eV and  $\varepsilon_{\text{inner}} = 6.5$  eV (solid coral). 3) Minimisation of  $\tilde{\Omega}$  only (MLWF) in the projected subspace (solid turquoise). 4) No minimisation (proj-ONLY) (solid blue). The DFT band-structure is also shown for reference (dotted black). It is worth clarifying that regardless of the initial projections, after a full minimisation—solid red line in all three panels—the Wannier interpolation is extremely good, particularly for the valence manifold. In fact, the three methods give almost indistinguishable results.

## Supplementary Note 2

In [S1](#) we report, for every element appearing in at least one structure used in this work, the number of valence electrons and the atomic pseudo-orbitals included in the pseudopotential files used in the simulations discussed in this work.

Table S1: List of number of valence electrons included in the pseudopotential ( $Z_{\text{val}}$ ) and atomic pseudo-orbitals included in the pseudopotential file (1s refers to an atomic  $s$  pseudo-orbital without radial nodes,  $2p$  to an atomic  $p$  pseudo-orbital with one radial node, ...)

Symbol	$Z_{\text{val}}$	Pseudo-orbitals	Symbol	$Z_{\text{val}}$	Pseudo-orbitals
H	1	1s	Br	7	1s, 1p
He	2	1s	Kr	8	1s, 1p
Li	3	1s, 1p, 2s	Rb	9	1s, 1p, 2s
Be	4	1s, 1p, 2s	Sr	10	1s, 1p, 1d, 2s, 2p
B	3	1s, 1p	Y	11	1s, 1p, 1d, 2s, 2p
C	4	1s, 1p	Zr	12	1s, 1p, 1d, 2s, 2p
N	5	1s, 1p	Nb	13	1s, 1p, 1d, 2s
O	6	1s, 1p	Mo	14	1s, 1p, 1d, 2s
F	7	1s, 1p	Ru	16	1s, 1p, 1d, 2s
Ne	8	1s, 1p	Rh	17	1s, 1p, 1d, 2s
Na	9	1s, 1p, 2s	Pd	18	1s, 1p, 1d, 2s
Mg	2	1s, 1p	Ag	19	1s, 1p, 1d, 2s
Al	3	1s, 1p	Cd	12	1s, 1p, 1d
Si	4	1s, 1p	In	13	1s, 1p, 1d
P	5	1s, 1p	Sn	14	1s, 1p, 1d
S	6	1s, 1p	Sb	15	1s, 1p, 1d
Cl	7	1s, 1p	Te	6	1s, 1p

Table S1 continued

Symbol	$Z_{\text{val}}$	Pseudo-orbitals	Symbol	$Z_{\text{val}}$	Pseudo-orbitals
Ar	8	1s, 1p	I	7	1s, 1p
K	9	1s, 1p, 2s, 2p	Xe	18	1s, 1p, 1d
Ca	10	1s, 1p, 1d, 2s	Cs	9	1s, 1p, 1d, 2s, 2p
Sc	11	1s, 1p, 1d, 2s	Ba	10	1s, 1p, 2s
Ti	12	1s, 1p, 1d, 2s	Hf	12	1s, 1p, 1d, 2s
V	13	1s, 1p, 1d, 2s	Ta	13	1s, 1p, 1d, 2s, 2p
Cr	14	1s, 1p, 1d, 2s	W	14	1s, 1p, 1d, 2s, 2p
Mn	15	1s, 1p, 1d, 2s, 2p	Re	15	1s, 1p, 1d, 2s, 2p
Fe	16	1s, 1p, 1d, 2s, 2p	Os	30	1s, 1p, 1d, 1f, 2s, 2p
Co	17	1s, 1p, 1d, 2s, 2p	Ir	15	1s, 1p, 1d, 2p
Ni	18	1s, 1p, 1d, 2s, 2p	Pt	16	1s, 1p, 1d, 2p
Cu	19	1s, 1p, 1d, 2s, 2p	Au	19	1s, 1p, 1d, 2s
Zn	20	1s, 1p, 1d, 2s, 2p	Hg	20	1s, 1p, 1d, 2s
Ga	13	1s, 1p, 1d	Tl	13	1s, 1p, 1d
Ge	14	1s, 1p, 1d	Pb	14	1s, 1p, 1d
As	5	1s, 1p	Bi	15	1s, 1p, 1d
Se	6	1s, 1p			

---

\* Corresponding author

- <sup>1</sup> Giannozzi, P. *et al.* Advanced capabilities for materials modelling with Quantum ESPRESSO. *Journal of Physics: Condensed Matter* **29**, 465901 (2017).
- <sup>2</sup> Damle, A. & Lin, L. Disentanglement via entanglement: A unified method for wannier localization. *Multiscale Modeling & Simulation* **16**, 1392–1410 (2018).
- <sup>3</sup> Vanderbilt, D. Soft self-consistent pseudopotentials in a generalized eigenvalue formalism. *Phys. Rev. B* **41**, 7892–7895 (1990).
- <sup>4</sup> Aquilante, F., Bondo Pedersen, T., Sánchez de Merás, A. & Koch, H. Fast noniterative orbital localization for large molecules. *The Journal of Chemical Physics* **125**, 174101 (2006).
- <sup>5</sup> Aquilante, F. *et al.* *Cholesky Decomposition Techniques in Electronic Structure Theory*, 301–343 (Springer Netherlands, Dordrecht, 2011).